Journal of Applied Physics ARTICLE pubs.aip.org/aip/jap

# Ballistic transport enhanced heat convection at nanoscale hotspots

Cite as: J. Appl. Phys. **136**, 164306 (2024); doi: 10.1063/5.0221352
Submitted: 31 May 2024 · Accepted: 12 October 2024 ·
Published Online: 28 October 2024



Shen Xu,[1,2] Yanru Xu,[1] Jingchao Zhang,[3] Jianshu Gao,[1] Xinwei Wang,[4] Xin Zhang,[5] and Yanan Yue[1,6,a)]

## AFFILIATIONS

[1]School of Power and Mechanical Engineering, Wuhan University, Wuhan, Hubei 430072, China
[2]School of Mechanical and Automotive Engineering, Shanghai University of Engineering Science, Shanghai 201620, China
[3]NVIDIA AI Technology Center (NVAITC), Santa Clara, California 95051, USA
[4]Department of Mechanical Engineering, Iowa State University, Ames, Iowa 50010, USA
[5]Department of Mechanical Engineering, Boston University, Boston, Massachusetts 02215, USA
[6]Department of Mechanical and Manufacturing Engineering, Miami University, Oxford, Ohio 45056, USA

**Note:** This paper is part of the special topic, Thermal Transport in 2D Materials.
[a)]**Author to whom correspondence should be addressed:** yyue@whu.edu.cn. **Tel.:** 86 27-68778876.

## ABSTRACT

Along with device miniaturization, severe heat accumulation at unexpected nanoscale hotspots attracts wide attentions and urges efficient thermal management. Heat convection is one of the important heat dissipating paths at nanoscale hotspots but its mechanism is still unclear. Here shows the first experimental investigation of the convective heat transfer coefficient at size-controllable nanoscale hotspots. A specially designed structure of a single-layer graphene supported by gold-nanorod array is proposed, in which the gold nanorods generate hundreds of nanometers heating sources under laser irradiation and the graphene layer works as a temperature probe in Raman thermometry. The determined convective heat transfer coefficient (1928+155 −147 $W m^{-2} K^{-1}$ for the 330 nm hotspot and 1793+157 −159 $W m^{-2} K^{-1}$ for the 240 nm hotspot) is about three orders of magnitude higher than that of nature convection, when the simultaneous interfacial heat conduction and radiation are carefully evaluated. Heat convection, thus, accounts to more than half of the total energy transferred across the graphene/gold nanorods interface. Both the plasmon induced nanoscale hotspots and ballistic convection of air molecules contribute to the enhanced heat convection. This work reveals the importance of heat convection at nanoscale hotspots to the accurate thermal design of miniaturized electronics and further offers a new way to evaluate the convective heat transfer coefficient at nanoscale hotspots.





## I. INTRODUCTION

The increasing power density in condensed integrated circuits and transistors brings an urgent need to explore thermal dissipation mechanism in confined spaces.[1,2] Besides mass heat accumulation, unexpected hotspots occurring at micro/nanostructures could strongly elevate local temperature and cause material deterioration and even device failure. When the characteristic length of these hotspots are at the scale of the surrounding media's phonon mean free path (MFP), the local thermal transport switches from the diffusion regime to the ballistic regime.[3] Studies have shown the frequent occurrence of ballistic behavior of thermal transport at micro/nanoscale hotspots,[4] which is greatly different from the macroscale heat transfer. Taking the ballistic heat conduction as an example, the effective thermal conductivity ($\kappa$) of the local media is obviously lower than its bulk value.[5]

Convection thermal transport plays a critical role in heat removal due to the existence of air surrounding the electronic devices.[6] Studies have shown that the convection thermal transport of water flow at microscale differs from macroscale.[7] However, as the dimension is down to the micro/nanoscale, reported results are scarce due to the measurement difficulties at such extreme scales.[8] Raman thermometry is a well-established approach for small-scale

temperature probing, in which temperature of the small scale could be accurately measured by evaluating the Raman shift of the characteristic Raman peaks of the local materials excited by Raman excitation laser. The focal diameter of the Raman excitation laser could be as small as 500 nm. For nano-materials and structures smaller than 500 nm having strong Raman scatterings could further increase the spatial resolution for temperature probing. These material-specific Raman peaks could also be captured using the same approach, such as 135 nm diameter porous silicon membrane and quantum dots.[9,10] The utilization of high-resolution Raman thermometry could also obtain the temperature at nanoscale hotspots surrounded by air molecules.

In this work, a specially designed tip-patterned substrate under Raman laser irradiation is used to generate hotspots and Raman scatterings. Raman thermometry can be combined to create a tip-enhanced Raman thermometry for hotspots generation and measurements.[11] By using experimental and numerical approaches, a tip-enhanced Raman thermometry is created to directly measure the interface thermal conductance and convective heat transfer coefficient at nanoscale hotspots. A periodic Au nanorods array is fabricated and utilized as resupinate tips to create hotspots based on their plasmonic effect under laser irradiation.[12,13] To be specific, the localized surface plasmon resonance of the gold nanorods under the 532 nm laser irradiation enhances the local electromagnetic field so as to the absorption in a single-layer graphene on the top of the nanorod. The heat transfer mechanism is then investigated in the graphene supported to reveal the importance of ballistic transport enhanced heat convection at nanoscale hotspots.

## II. EXPERIMENTAL DETAILS

### A. Preparation of Au nanorod array

Template-assisted lithography is used to prepare a gold nanopattern on the silicon substrate. The procedures are shown in Fig. 1. A commercial ultrathin alumina membrane (UTAM) works as a template, which has multiple pores with a thickness of 650 nm, diameter of 350 nm, and periodicity of 450 nm. The polymethyl methacrylate (PMMA) is the support material.[14] After being coated with a 200 nm gold coating and then peeled off the UTAM, the Au nanorods are fabricated in the masked substrate. On the rest uncovered silicon substrate, a continuous Au film (AuF) is simultaneously deposited.

Figure 2 shows structure characterization of the Au nanorods (Au330) on the silicon substrate. The nanorods have an average diameter of 330 nm, a height of 200 nm, and a periodicity of 450 nm. A CVD prepared single-layer graphene (Gr) with the dimension of $1 \times 1\ cm^2$ is later transferred onto Au330/Si [Fig. 2(b)]. Compared with the close contact between graphene and gold sputter-coating film/silicon substrate (AuF/Si), the contact areas between graphene and Au330/Si are restricted to the top areas of the gold nanorods.

Another sample have the Au nanorods with a diameter of 240 nm on the silicon substrate (Au240/Si) is later fabricated. The

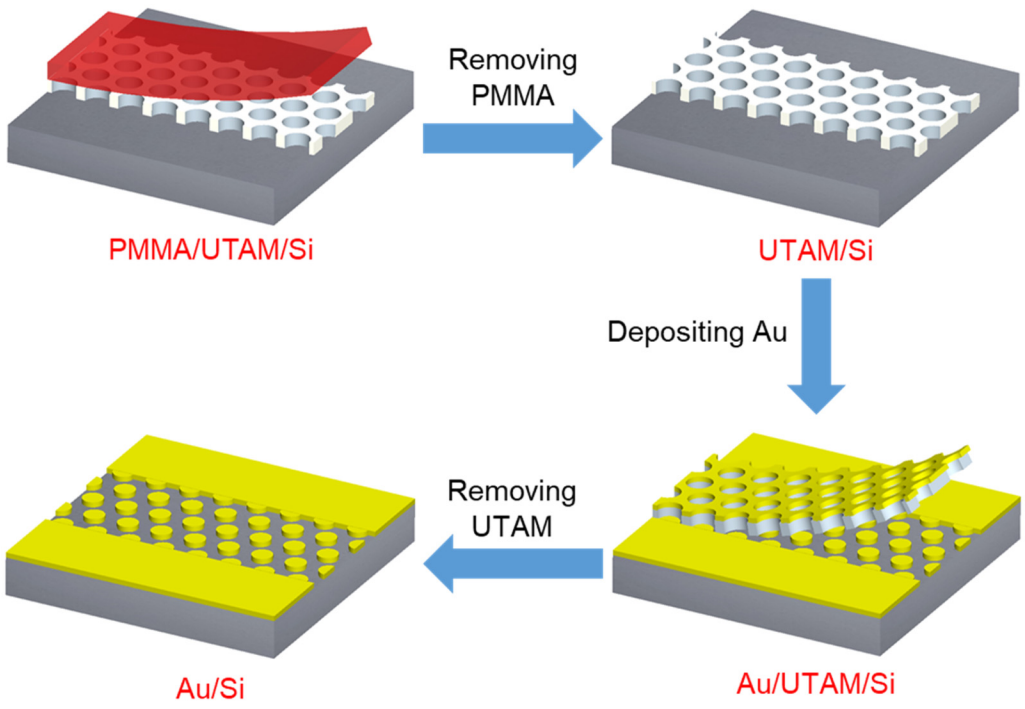


**FIG. 1.** The schematic of preparation processes of Au nanorod array.

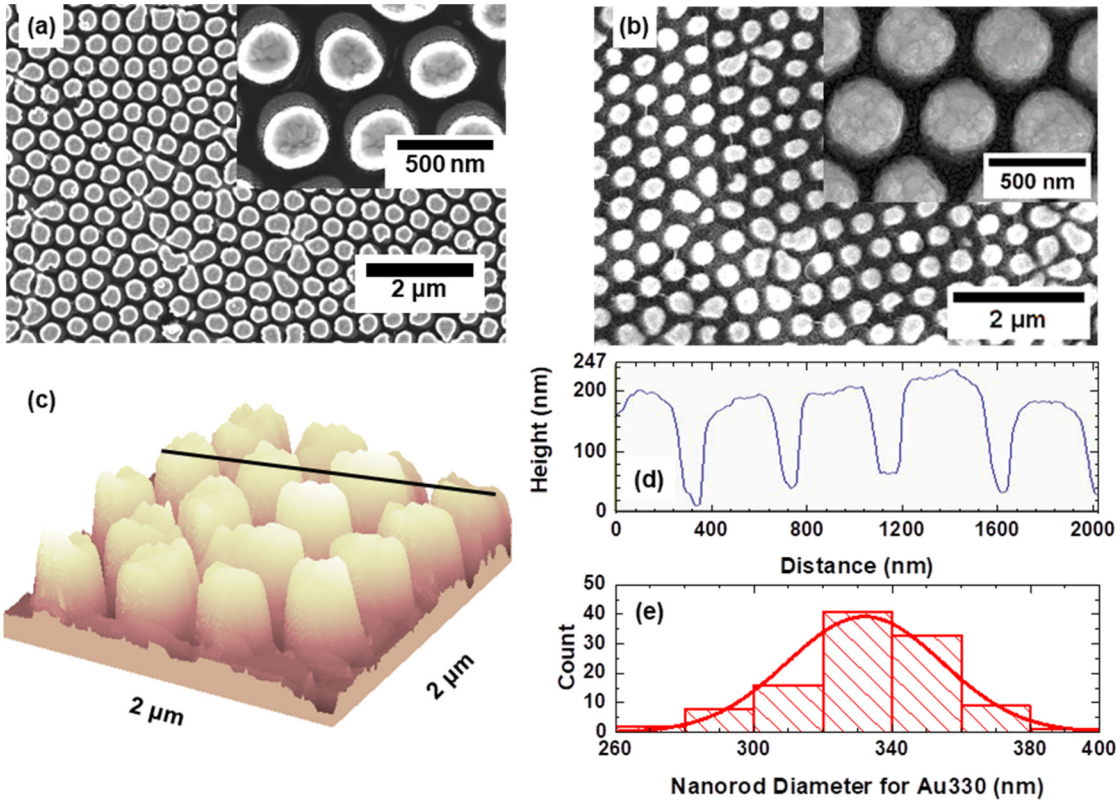


**FIG. 2.** SEM images of (a) Au330/Si and (b) graphene on Au330/Si. (c) 3D AFM image of Au330/Si. (d) Longitudinal section analysis of the nanorod height for Au330 in accordance with the evaporation film thickness. (e) Histogram of diameter distribution for Au330.



preparation process of Au240/Si is similar as that of Au330/Si. The used UTAM has pores with a diameter of 260 nm, a periodicity of 450 nm, and a thickness of 650 nm. The thickness of the evaporated Au film is 100 nm. The SEM image in Fig. 3(a) shows that Au240 are patterned in a long-range hexagonal array. The average diameter of the nanorods is $240 \pm 26\ \text{nm}^2$ shown in Fig. 3(b), the periodicity of the nanorods is 450 nm, and the averaged height of the nanorods shown in Figs. 3(c) and 3(d) is in accordance with the evaporation film thickness. After the Au240/Si is prepared, a single-layer graphene is also transferred to both the top of the nanorods region and continous Au film region. SEM images of Gr/Au240/Si in Fig. 3(e) show a layer graphene suspended on the top surface of the Au240 array.

### B. Measurements of temperature rise of graphene

Graphene has a strong Raman scattering and is a good candidate for temperature probing around the top of Au nanorods. Thus, a Raman spectrometer (B&W Tek) with a 532 nm diode laser is first used for temperature coefficient calibration of graphene Raman signal. The focusing laser spot has a diameter of $\sim 50\,\mu\text{m}$ at the tested surface with a power of 30 mW. Temperature of the sample is precisely controlled by a ceramic heater over the range from 300 to 365 K. An integration time of 240 s is applied to ensure the temperature measurement accuracy. As shown in Fig. 4(a), the peak wavenumber is determined by fitting *G-band* using a single Lorentzian shape.[15] The Raman signal of graphene is collected at least three times for averaging. All the experiments are repeated twice for averaging. The temperature coefficient calibration result is shown in Fig. 4(b). As the temperature increases, the peak wavenumber of the *G-band* shifts to a lower wavenumber. The temperature coefficient of the *G-band* is determined as $-0.021 \pm 0.005\ \text{cm}^{-1}\,\text{K}^{-1}$, in good agreement with the reported value ($-0.025\ \text{cm}^{-1}\,\text{K}^{-1}$).[16]

For temperature rise measurement of graphene on AuF/Si and Au330/Si, it is conducted using the same Raman spectrometer, but the incident Raman laser serves as the exciting and heating source simultaneously. The laser power per unit area is adjusted from 0.006 to $0.015\ \text{mW}\,\mu\text{m}^{-2}$, while the integration time varies from 50 to 20 s to guarantee strong Raman signals. In Figs. 5(a) and 5(b), the *G-band* for both Gr/AuF/Si and Gr/Au330/Si shifts to left due to heating induced temperature rise. However, under the same heating level, the shift of the peak wavenumber of the *G-band* for two samples is different. After excluding the effect of the integration

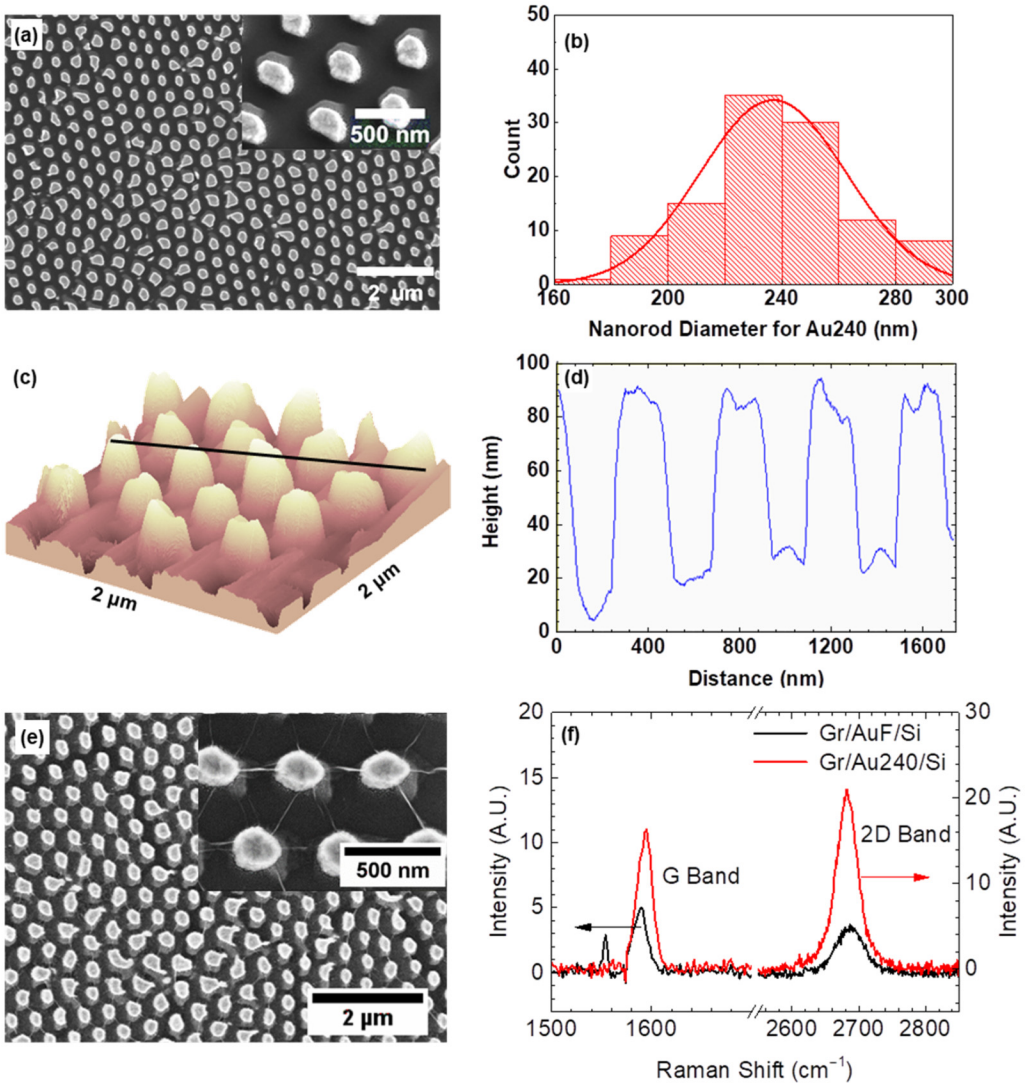


**FIG. 3.** Au240/Si substrate characterization. (a) SEM image of Au240/Si. (b) Histogram of diameter distribution for Au240. The average diameter of the nanorods is 240 nm. They range in a hexagonal array with a periodicity of 450 nm. (c) 3D AFM image of Au240/Si. (d) Longitudinal section analysis of nanorods height for Au240, in accordance with the evaporation film thickness. (e) SEM images of Gr/Au240/Si. (f) Raman spectrum of Gr/AuF/Si and Gr/Au240/Si.

time, the obtained *G-band* is fitted to determine the graphene temperature. To alleviate the measurement uncertainties, the change in peak wavenumber against laser power is applied to extract the graphene temperature rise. The determined peak wavenumber shift against laser power for two samples is shown in Figs. 3(c) and 3(d). The average temperature rise per unit laser power is $1.38 \pm 0.62\ \mathrm{K\,mW^{-1}}$ for Gr/AuF/Si and $3.52 \pm 1.01\ \mathrm{K\,mW^{-1}}$ for Gr/Au330/Si. It is obviously that the temperature in Gr/Au330/Si is much higher than that in Gr/AuF/Si, when applying the same level heating power. The nanorods induced optical field enhancement and nanoscale heat transfer mechanism may account for this difference.

## III. RESULTS AND DISCUSSION

### A. Electromagnetic field simulation of Au nanorod array

Under the irradiation of the laser with a wavelength in the visible range, the gold nanostructures could generate localized surface plasmons around the nanostructures and enhance the local electromagnetic field due to the localized surface plasmon resonance (LSPR). Therefore, the local optical field adjacent to the top of the nanorods will be enhanced, so as to the absorbed laser energy by the graphene attached to the top of those nanorods, when compared with the laser absorption of the graphene on AuF/Si. As shown in

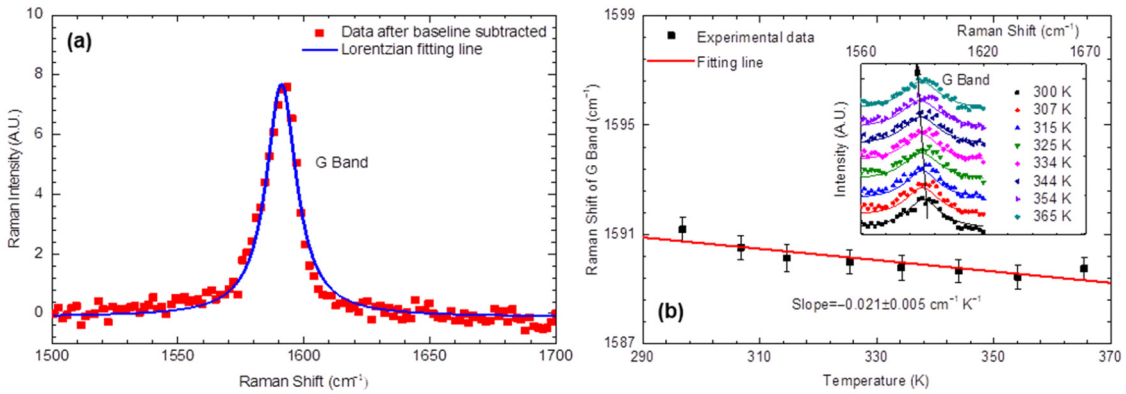


**FIG. 4.** (a) The typical *G-band* of graphene and its Lorentzian fitting line. (b) Calibration result of *G-band*. The inset depicts *G-band* line at temperatures ranging from 300 to 365 K.

Fig. 6, the finite-difference time-domain (FDTD) simulation is performed to define the LSPR-induced enhancement of the incident optical field. In the FDTD model, a hexagonal array of Au nanorods is used for representing the array of Au330. The nanorod has a diameter of 330 nm, a height of 200 nm, and the periodicity of cylinders is 450 nm, which are in accordance with the exact dimensions of the prepared Au330. A plane wave with the wavelength ranging from 400 to 800 nm comes from the top of the domain and is

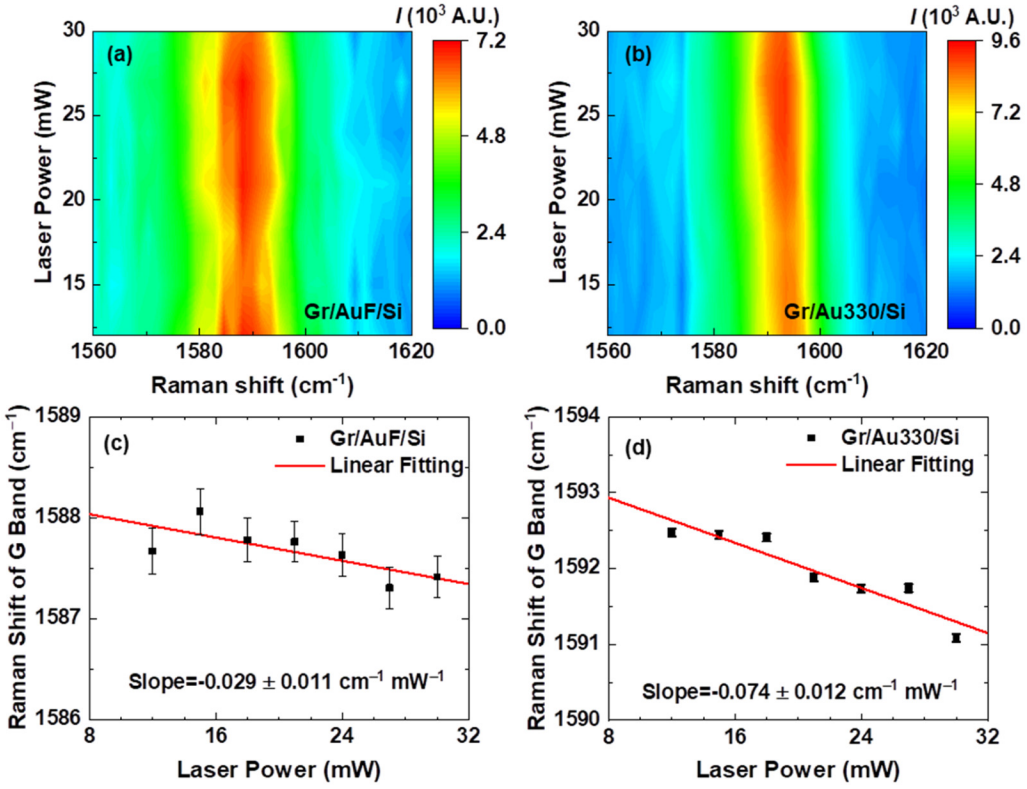


**FIG. 5.** Raman based temperature measurement. The contour map of Raman peak for *G-band* vs laser power for (a) Gr/AuF/Si and (b) Gr/Au330/Si. Linear fitting of the *G-band* peak wavenumber against the laser power for (c) Gr/AuF/Si and (d) Gr/Au330/Si in the heating range from 12 to 30 mW.

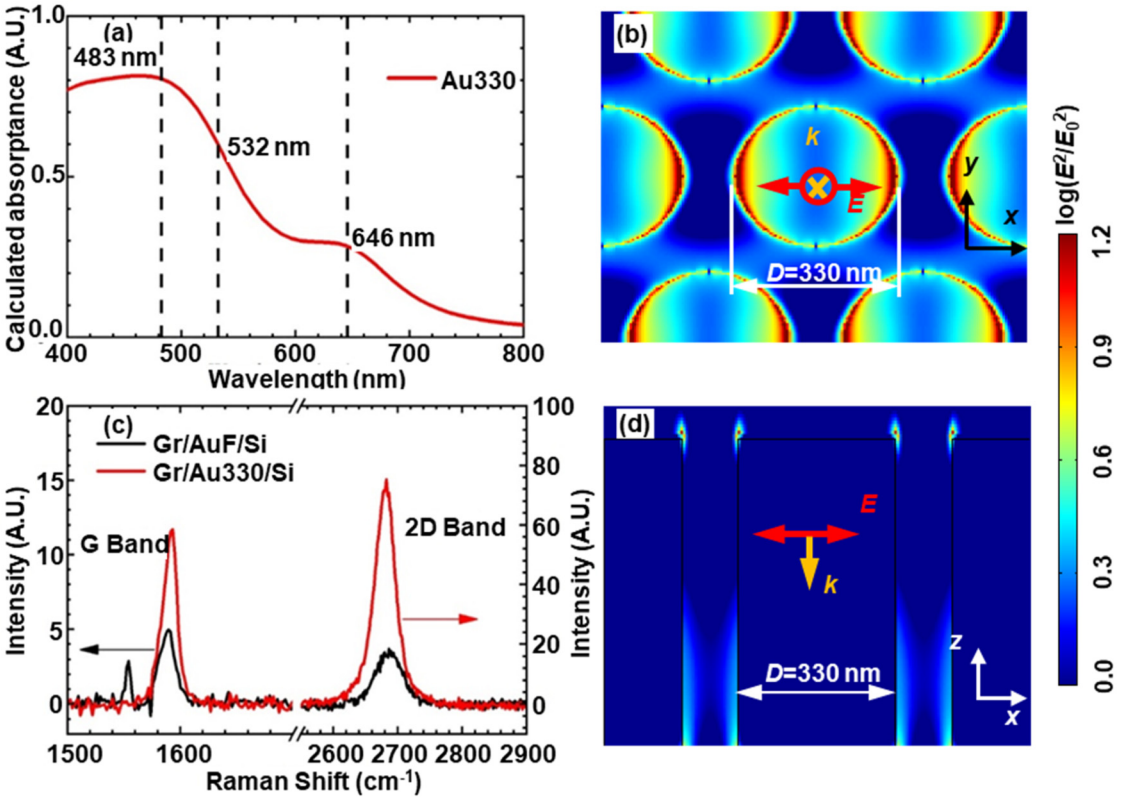


**FIG. 6.** Surface enhancement on the Au nanorods. (a) The simulated extinction spectrum of Au330. The electric intensity enhancement distribution (on a log scale) on (b) the top surface of gold nanorods and (d) the central *xz* plane at 532 nm laser excitation. (c) Comparison in Raman spectra of graphene on AuF/Si and Au330/Si. An enhancement factor of 11.8 is observed for the G peak of graphene on Au330/Si.



normal to the top of the rods. Its polarization direction is along the *x* axis. The computational domain is $900 \times 779 \times 2000\ \text{nm}^3$ ($x \times y \times z$). Periodic boundary conditions are applied to the *x*–*y* plane and perfectly matched layer boundary conditions are applied to the *z* direction. The distance from the nanorods to the absorbing boundary is set to be larger than one half of the incident wavelength. The entire domain is adaptively divided into cuboid elements with their side length less than 1/26 of the incident wavelength. For simplicity, the amplitude of the incident electric field ($E_0$) is set to be $1\ \text{V m}^{-1}$. The permittivities of gold are obtained from the reported data by Johnson and Christy.[17] The calculated Raman enhancement factor is estimated as the second power of electric intensity enhancement factor based on the electromagnetic enhancement mechanism.[18]

To determine the absorption of incident energy (extinction, *A*) by the gold layer, reflection (*R*) and transmission (*T*) on the gold film are simulated. The extinction is calculated by $A = 1 - R - T$. The electric field intensity distribution around Au330 is also simulated by using the FDTD model described above. LSPR (localized surface plasmon resonance) generated by Au330 enhances the Raman intensity by a factor of 11.8 and 20.4 for the *G-band* and the *2D-band*, respectively. The enhancement distribution induced by Au330 can be pictured by the simulated electromagnetic field. The Au330 absorption [Fig. 6(a)] decreases from 0.8 to 0.04 as the incident wavelengths increasing from 400 to 800 nm with two plasmonic bands. Figures 6(b) and 6(d) show that the top surface electric field at the nanorod edge is greatly intensified generating theoretical Raman enhancement factor of 9.3 for the *G-band* at 532 nm.[19,20]

## B. Interfacial thermal conductance between Au and graphene

In addition to the LSPR-induced optical field enhancement, the substrate structure is another main factor contributing to this difference. Under the steady state laser heating, the generated thermal energy in the graphene layer then dissipates to the surroundings through heat conduction, convection, and radiation. The schematic experimental setup and heat transfer mechanism for Gr/AuF/Si and Gr/Au330/Si are shown in Fig. 7(a). The large heating spot size, which is larger than the phonon mean free path in graphene,[21] ensures that the temperature in the spot region will be uniform. Theoretically, for Gr/AuF/Si [Fig. 7(b)], the main heat dissipation pathways are conducting along the in-plane direction in the graphene layer ($q_{f1}$) and across the Gr/Au interface

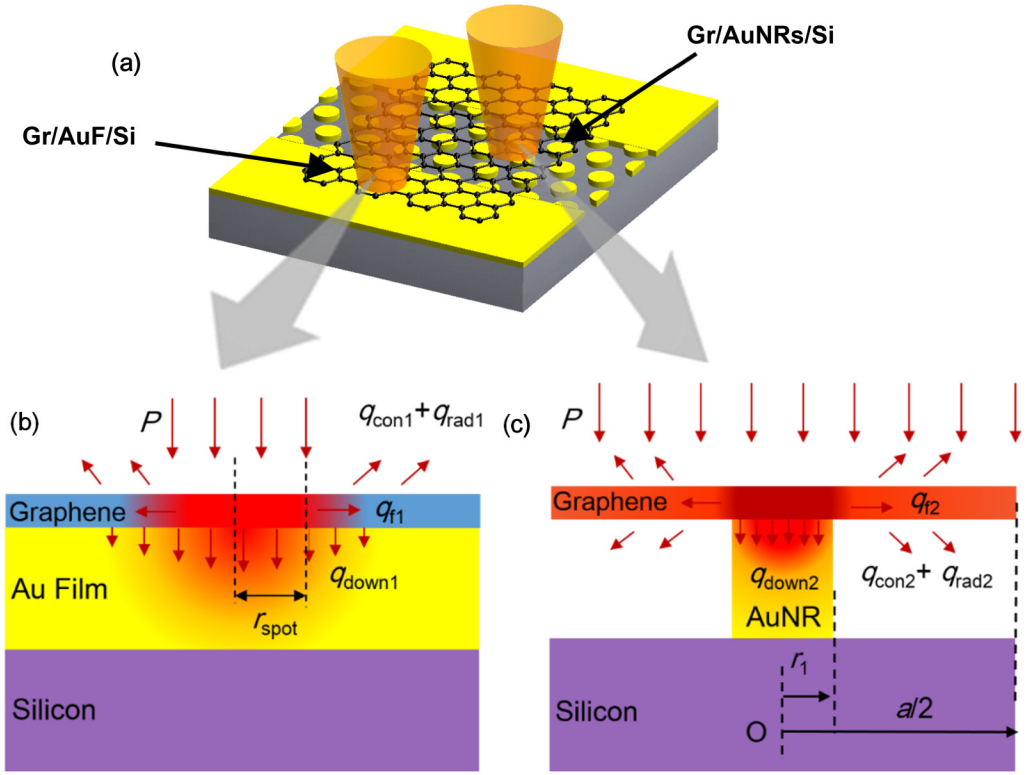


**FIG. 7.** Different heat transfer mechanisms in two structures. (a) The schematic of laser heating on Gr/AuF/Si and Gr/Au330/Si. Two different mechanisms of thermal transport in (b) Gr/AuF/Si and (c) Gr/Au330/Si under the laser heating.



($q_{down1}$) with some dissipation through thermal radiation ($q_{rad1}$) and convection ($q_{con1}$) from the top surface of the graphene layer. For Gr/Au330/Si, the thermal transport path is a little different. Since only a portion of the bottom surface of the graphene layer is contacted by Au330, the rest suspended portion is surrounded by air at both top and bottom surfaces shown in Fig. 7(c). Thus, heat convection and radiation will occur from both top surface and exposed bottom surface of the graphene layer. To investigate the convective thermal transport from graphene on Au330/Si, the thermal conduction across the Gr/Au interface must be studied first.

Given that Gr/AuF/Si and Gr/Au330/Si are prepared in the same batch, the roughness of the top surface for AuF and Au330 should be similar. Furthermore, Au330 have the same height as AuF has. They densely distribute on the Si substrate between two large gold films, so the transferred graphene layer could be well supported by Au330. We assume that the contact between the graphene layer and Au330 is in the same condition as that between graphene and AuF. Then, the interfacial thermal conductance ($G_{Gr/Au}$) between the graphene layer and the Au film is measured first in Gr/AuF/Si.

Based on the experimentally measured temperature rise of graphene on AuF/Si, the interface thermal conductance can be solved with the assistance of the numerical finite element (FE) method. In the FE model for Gr/AuF/Si in Fig. 8(a), a uniform heat generation source $\dot{q}_{Gr1}$ is applied to the graphene for the reason that the heating spot is large enough and the temperature is uniform in the spot region. It has the expression as $\dot{q}_{Gr1} = I\alpha_{Gr/Au}/t_{Gr}$, where $I$ is the incident laser intensity (0.015 mW $\mu$m$^{-2}$), $\alpha_{Gr/Au}$ is the absorption of graphene on Au film, and $t_{Gr}$ is the thickness of the single-layer graphene (~0.34 nm).[22] The absorption of the suspended single-layer graphene is reported to be 2.3% in the visible light wavelength range.[23] However, in the case of the supported graphene, the incident laser will reflect at the interface between the graphene and the gold film. Given that 70% of the laser energy is reflected by Au film,[24] after transmitting through the supported graphene layer again, $\alpha_{Gr/Au}$ is considered to be 3.9% in the FE model. The temperature of the surrounding boundary of graphene is kept at room temperature (300 K). Convective heat transfer from graphene to air is considered. Radiative heat transfer to surroundings from the graphene surface is negligible because it is estimated to be 0.002% of the total heat dissipation in graphene considering that the emissivity of graphene is 0.023 based on the Stefan–Boltzmann law. The constant pressure heat capacity and density of graphene is set as 750 J (kg K)$^{-1}$ and 2200 kg m$^{-3}$.[25] The thermal conductivity of graphene on the substrate $\kappa_{Gr}$ is adopted as 179 W m$^{-1}$ K$^{-1}$.[26] Though the thermal conductivity is large, the cross-sectional area

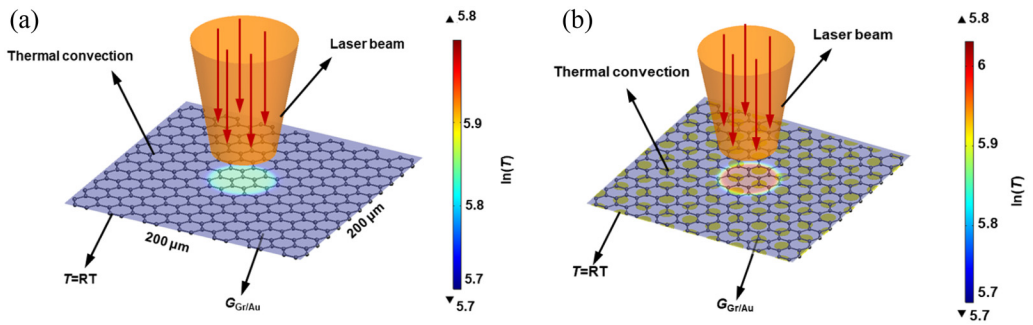


**FIG. 8.** (a) The schematic of the FE model for the determination of the interfacial thermal conductance ($G_{Gr/Au}$) between graphene and the Au film. (b) The schematic of the FE model for graphene on Au330/Si and the simulated temperature distribution of graphene on Au330/Si with the average temperature rise of graphene within the spot region as 105.7 K.

is small due to the atomic thickness of the single layer. Heat can pass through the interface to the Au/Si substrate and transfer to Au nanorods.

In the simulation, when the average temperature rise of graphene within the heating spot matches the experimentally result, the interface thermal conductance between the graphene and the gold film $G_{Gr/Au}$ is then determined to be $1.35+0.37-0.33 \times 10^4$ W m$^{-2}$ K$^{-1}$. This value is the same as that of the unconstrained graphene/4H SiC interface[27] but is much lower than that reported for the intercalated graphene interface.[28] It indicates the existence of a gap between graphene and AuF/Si. Molecular dynamics simulations also confirm that the conductance decreases exponentially with increasing gap thickness. This separation weakens the interatomic forces and energy coupling between the two materials. Ripples and wrinkles in graphene as well as chemical residues introduced during the preparation process will be the main cause of interfacial separation. In addition, the different thermal expansion behavior of graphene and gold may cause thermal mismatch[27] at the interface and further increase their separation distance. We evaluate the effect of the reference thermal conductivity of the graphene $\kappa_{Gr}$ on the determined $G_{Gr/Au}$. It is found that the variation of $G_{Gr/Au}$ (0.15 W m$^{-2}$ K$^{-1}$) raised by $\kappa_{Gr}$ is much less than the uncertainty of $G_{Gr/Au}$ in the temperature measurement of graphene, when $\kappa_{Gr}$ varies from 179 to 600 W m$^{-1}$ K$^{-1}$.[29]

### C. Convective heat transfer coefficient at graphene nanoscale hotspot

The surface temperature of graphene on Au330/Si is measured using the same Raman method and its Raman intensity contour map against incident power is shown in Fig. 5(b). Combined with the temperature coefficient of *G-band* Raman shift (−0.021 cm$^{-1}$ K$^{-1}$), the temperature rise of graphene is determined by the slope of the fit of the *G-band* Raman shift to the laser power (−0.074 cm$^{-1}$ mW$^{-1}$), as shown in Fig. 5(d). The average local temperature rise within the laser irradiated region is 105.7 ± 2.4 K at a laser power of 30 mW, which is much higher than 41.4 ± 9.5 K for graphene on AuF/Si, indicating that graphene is additionally heated by the Au330-induced hotspots. For the graphene on Au330/Si, the contact area of the graphene/Au330 interface is reduced due to the discontinuity of the upper surface of the Au330 layer, and the generated heat can only be conducted through the contact area. The low thermal conductance at the loosely contacted interface limits the heat dissipation and raises the temperature of the graphene layer. By improving the photon absorption in graphene, the confined electric field in the local region around the nanorods provides an opportunity to generate nanoscale hotspots in graphene.

The schematic of the simulation model for graphene on Au330/Si is shown in Fig. 8(b). A uniform heat generation $\dot{q}_{Gr2}$ is applied in graphene within the laser irradiated area, which is expressed as $\dot{q}_{Gr2} = I\alpha_{Gr}M/t_{Gr}$, where $\alpha_{Gr}$ is the absorptance of single-layer graphene, 2.3%. $M$ is the calculated electric intensity enhancement factor, $M = 3.1$. $I$ is the incident laser intensity (0.015 mW $\mu$m$^{-2}$). The temperature of surrounding boundary is set as room temperature. Thermal convection conditions are used on the top surface and the bottom suspended region of graphene. The radiative heat loss is around 0.002%–0.003% of the total heat dissipation of graphene and is still neglected in this model. When the average temperature rise of the graphene within the laser spot matches the experimental result, the convective heat transfer coefficient ($h$) around graphene nanoscale hotspot on gold nanopattern is determined to be $1928+155-147$ W m$^{-2}$ K$^{-1}$. The percentage of the convective heat loss around the graphene for Gr/Au330/Si is then calculated to be about 26.6%. High heat convection effect and low interfacial thermal conductance prevent large amount of thermal energy from conducting to the Au nanorod substrates.

### D. Parallel measurement on Au240

The hotspots generated by the LSPR effect correspond to the size of the nanorods. In thermal measurement, nanorods work as nanoheaters that heat the graphene layer and some of the heat dissipates into the air molecules surrounding the nanorods. When the size of nanoheaters is close to the mean free path of air molecules at room temperature and pressure, the size effect will enhance the convective heat transfer coefficient $h$ by several orders of magnitude.[7] To confirm this speculation, we use the other gold-nanorod pattern

(Au240), whose nanorods have a diameter of 240 nm, a height of 100 nm, and a period of 450 nm, in accordance with Au330.

Raman spectrum of Gr/Au240/Si in Fig. 3(f) illustrates the *G-band* around 1589.86–1593.39 $cm^{-1}$ and *2D-band* around 2682.67–2686.23 $cm^{-1}$.[30] The absence of *D band* indicates few defects in transferred graphene on Au240/Si. The ratio $I_{2D}/I_G$ is 1.28, indicating the nature of the monolayer.[15] *G-band* exhibits an upshift of 5 $cm^{-1}$ with respect to graphene on AuF/Si due to the doping effect. The downshift of *2D-band* of graphene on Au240 may be attributed to the doping of graphene by the Au nanorods and compressive strain.[31–33]

As shown in Fig. 3(f), the Raman intensity of *G-band* and *2D-band* of graphene on Au240/Si is enhanced by a factor of 3.3 and 5.7, respectively. This enhancement factor is comparable to the literature-reported value for 140–210 nm Au dots.[34] The simulated extinction spectrum in Fig. 9(a) of Au240 exhibits plasmon bands in the range of 400–800 nm with the peak wavelengths at 432 and 536 nm. It agrees well with the measured results of gold nanoparticles with the similar size,[35] confirming the existence of the plasmonic effect of the Au nanorods.[19,20,34] The simulated electric field around Au240 shown in Figs. 9(b) and 9(d) illustrates that the enhanced electric field occurs at the edges on the top surface of Au240 and is confined in 10 nm scale along the *x* axis and 80 nm along the *y* axis. The region of electromagnetic field enhancement is more obvious and larger than that of Au330 in Fig. 6(d). Based on the mechanism of electromagnetic enhancement for surface enhanced Raman scattering,[36] the theoretical Raman enhancement factor of graphene induced by Au240 is calculated to be 3.0 at 532 nm, well agreeing with the experimental value.[19,20] The extremely concentrated electric field contributed a lot to the energy absorption in the graphene layer in sample Gr/Au330/Si, while the less concentrated electric field in Gr/Au240/Si may be the main reason causing lower electric field intensity.

Raman thermal measurement has been conducted on Gr/Au240/Si by varying the laser power under the excitation of the 532 nm diode laser. As shown in Fig. 9(c), the *G-band* wavenumber shifts linearly with the increment of the laser power. The fitted slope is $-0.057 \pm 0.009\ cm^{-1}\ mW^{-1}$. The local average temperature rise of graphene within the focal spot is $81.4 \pm 3.8$ K at 30 mW. The less concentrated electric field also causes a lower temperature rise in the 0.34 nm thick graphene layer in Gr/Au240/Si. The determined convective heat transfer coefficient ($h$) around the graphene on Au240/Si is 1793+157 −159 $W\,m^{-2}\,K^{-1}$. Considering the little geometric differences and measurement uncertainties,[28,37] this result is consistent with measured value of Gr/Au330/Si.

## E. Combination of nanoscale heating and ballistic effect

The combination of LSPR-induced nanoscale hotspot heating and ballistic convection effect of air molecules may be responsible for the high values of the measured convective heat transfer coefficients. The nanoscale hotspot puts air convection in transition regime and transfers heat in a ballistic manner. The heat transfer government of the surrounding air molecules over the nanostructure-induced hotspots can be defined by *Kn* number, which is the ratio of the mean free path $\lambda$ of air molecules[38] to the characteristic length of the hotspot. In the case of open-air measurements of Gr/Au330/Si, $\lambda$ of air molecules is 80 nm and the $l$ of gold nanorods is 330 nm. The resultant *Kn* is 0.24, which lies in the range of 0.01–10, indicating that the airflow regime over the hotspot belongs to the transition regime. Since



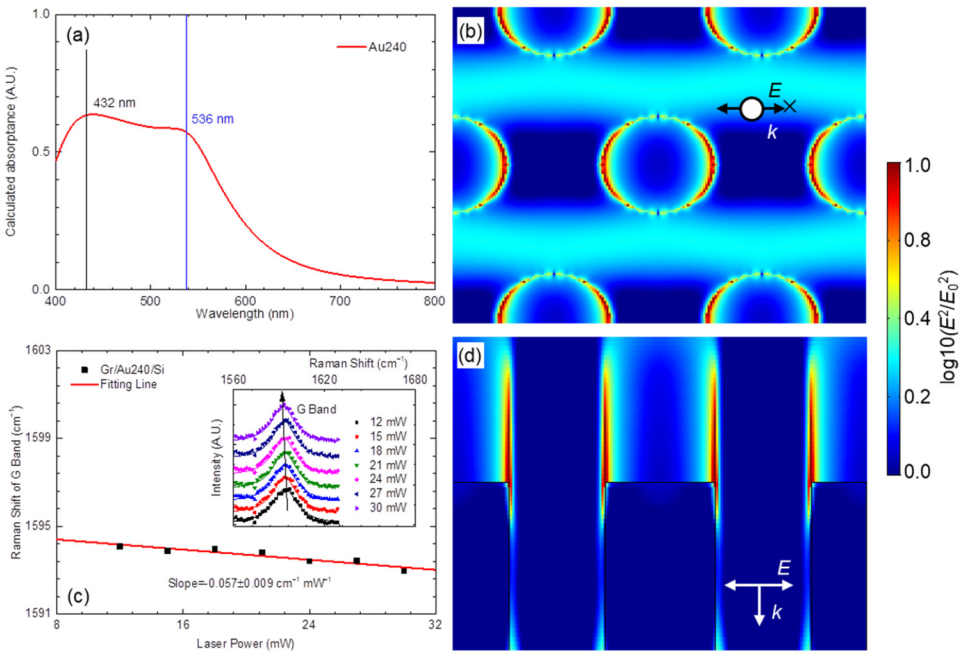


**FIG. 9.** (a) The simulated extinction spectrum of gold nanorods. The electric intensity enhancement distribution of (b) the top surface of gold nanorods and (d) the central *xz* plane. (c) Raman shift of the *G-band* vs laser power for Gr/A240/Si. The inset depicts *G-band* lines over the range of laser power from 12 to 30 mW.

the size of the hotspot is similar to the mean free path of air molecules, the probability of ballistic heat conduction of free air molecules may increase. Heat conduction through air molecules plays an important role instead of advection-based heat transfer,[37] leading to enhanced thermal convection.

The evaluation of heat dissipation based on the determined heat transfer coefficients demonstrates that convective heat loss accounts for 53%–100% of the total heat conduction from graphene to Au330/Si and Au240/Si through the interface. This high percentage indicates that the convective heat loss from the nanoscale hotspots in the graphene layers to the surrounding air is significant and cannot be neglected in the precise design of relevant thermal management systems. Meanwhile, the tip-enhanced Raman thermometry developed in this work offers a new methodology for measuring the convective heat transfer coefficient of the nanoscale hotspots.

## IV. CONCLUSION

In summary, the convective heat transfer coefficient of air molecules in the transition regime over the nanoscale hotspot is characterized using the tip-enhanced Raman thermometry. The experimental results show that the gold-nanorod-induced near-field effect (LSPR) enhances the Raman intensity and incident energy absorption, resulting in an LSPR-induced hotspot at the graphene layer. The temperature increase in the graphene layer is measured and used to reconstruct the heat transfer model in the sample and to determine the convective heat transfer coefficient over the hotspots. The determined average convective heat transfer coefficients, $1928+155\ -147\ \mathrm{W\,m^{-2}\,K^{-1}}$ for Gr/Au330 and $1793+157\ -159\ \mathrm{W\,m^{-2}\,K^{-1}}$ for Gr/Au240, indicate ballistic driven large convective heat transfer at the nanoscale hotspot. This tip-enhanced Raman thermometry provides a new method to experimentally quantify ballistic heat transport from nanoscale hotspots. The measurement results can be used as a guide for better thermal design and management.

## ACKNOWLEDGMENTS

The authors acknowledge the financial support from the National Key Research and Development Program (No. 2023YFE0120200), National Natural Science Foundation of China (NNSFC) (Nos. 52076156 and 52106220), and Science Fund for Distinguished Young Scholars of Hubei Province (No. 2022CFA076).

## AUTHOR DECLARATIONS

### Conflict of Interest

The authors have no conflicts to disclose.

### Author Contributions

**Shen Xu:** Funding acquisition (equal); Investigation (equal); Methodology (equal); Visualization (equal); Writing – original draft (equal). **Yanru Xu:** Conceptualization (equal); Investigation (equal); Methodology (equal); Visualization (equal); Writing – original draft (equal). **Jingchao Zhang:** Investigation (equal); Methodology (equal); Writing – original draft (equal). **Jianshu Gao:** Visualization (equal); Writing – original draft (equal). **Xinwei Wang:** Writing – review & editing (supporting). **Xin Zhang:** Writing – review & editing (equal). **Yanan Yue:** Conceptualization (equal); Funding acquisition (equal); Investigation (equal); Methodology (equal); Supervision (lead); Writing – review & editing (equal).

## DATA AVAILABILITY

The data that support the findings of this study are available within the article.

## REFERENCES

[1]N. Han, T. Viet Cuong, M. Han, B. Deul Ryu, S. Chandramohan, J. Bae Park, J. Hye Kang, Y.-J. Park, K. Bok Ko, H. Yun Kim, H. Kyu Kim, J. Hyoung Ryu, Y. S. Katharria, C.-J. Choi, and C.-H. Hong, "Improved heat dissipation in gallium nitride light-emitting diodes with embedded graphene oxide pattern," Nat. Commun. **4**, 1452 (2013).
[2]M. López-Suárez, I. Neri, and L. Gammaitoni, "Sub-kBT micro-electromechanical irreversible logic gate," Nat. Commun. **7**, 12068 (2016).
[3]A. Keerthi, A. K. Geim, A. Janardanan, A. P. Rooney, A. Esfandiar, S. Hu, S. A. Dar, I. V. Grigorieva, S. J. Haigh, F. C. Wang, and B. Radha, "Ballistic molecular transport through two-dimensional channels," Nature **558**, 420–424 (2018).
[4]Y. Hu, L. Zeng, A. J. Minnich, M. S. Dresselhaus, and G. Chen, "Spectral mapping of thermal conductivity through nanoscale ballistic transport," Nat. Nanotechnol. **10**, 701–706 (2015).
[5]G. Chen, "Non-Fourier phonon heat conduction at the microscale and nanoscale," Nat. Rev. Phys. **3**, 555–569 (2021).
[6]S. Chen, A. Moore, W. Cai, J. Won Suk, J. An, C. Mishra, C. Amos, C. W. Magnuson, J. Kang, L. Shi, and R. Ruoff, "Raman measurements of thermal transport in suspended monolayer graphene of variable sizes in vacuum and gaseous environments," ACS Nano **5**, 321–328 (2011).
[7]M. Mehrvand and S. A. Putnam, "Transient and local two-phase heat transport at macro-scales to nano-scales," Commun. Phys. **1**, 21 (2018).
[8]D. Halbertal, J. Cuppens, M. B. Shalom, L. Embon, N. Shadmi, Y. Anahory, H. R. Naren, J. Sarkar, A. Uri, Y. Ronen, Y. Myasoedov, L. S. Levitov, E. Joselevich, A. K. Geim, and E. Zeldov, "Nanoscale thermal imaging of dissipation in quantum systems," Nature **539**, 407–410 (2016).
[9]B. Graczykowski, A. El Sachat, J. S. Reparaz, M. Sledzinska, M. R. Wagner, E. Chavez-Angel, Y. Wu, S. Volz, Y. Wu, F. Alzina, and C. M. Sotomayor Torres, "Thermal conductivity and air-mediated losses in periodic porous silicon membranes at high temperatures," Nat. Commun. **8**, 415 (2017).
[10]F. Tebbenjohanns, M. L. Mattana, M. Rossi, M. Frimmer, and L. Novotny, "Quantum control of a nanoparticle optically levitated in cryogenic free space," Nature **595**, 378–382 (2021).
[11]A. M. Gilbertson, Y. Francescato, T. Roschuk, V. Shautsova, Y. Chen, T. P. H. Sidiropoulos, M. Hong, V. Giannini, S. A. Maier, L. F. Cohen, and R. F. Oulton, "Plasmon-induced optical anisotropy in hybrid graphene–metal nanoparticle systems," Nano Lett. **15**, 3458–3464 (2015).
[12]P. Wang, W. Zhang, O. Liang, M. Pantoja, J. Katzer, T. Schroeder, and Y.-H. Xie, "Giant optical response from graphene–plasmonic system," ACS Nano **6**, 6244–6249 (2012).
[13]W. Zhang, H. Liu, J. Lu, L. Ni, H. Liu, Q. Li, M. Qiu, B. Xu, T. Lee, Z. Zhao, X. Wang, M. Wang, T. Wang, A. Offenhäusser, D. Mayer, W.-T. Hwang, and D. Xiang, "Atomic switches of metallic point contacts by plasmonic heating," Light Sci. Appl. **8**, 34 (2019).
[14]H. Robatjazi, S. M. Bahauddin, L. H. Macfarlan, S. Fu, and I. Thomann, "Ultrathin AAO membrane as a generic template for sub-100 nm nanostructure fabrication," Chem. Mater. **28**, 4546–4553 (2016).

[15]D. Graf, F. Molitor, K. Ensslin, C. Stampfer, A. Jungen, C. Hierold, and L. Wirtz, "Spatially resolved Raman spectroscopy of single- and few-layer graphene," Nano Lett. **7**, 238–242 (2007).
[16]X. Tang, S. Xu, J. Zhang, and X. Wang, "Five orders of magnitude reduction in energy coupling across corrugated graphene/substrate interfaces," ACS Appl. Mater. Interfaces **6**, 2809–2818 (2014).
[17]P. B. Johnson and R. W. Christy, "Optical constants of the noble metals," Phys. Rev. B **6**, 4370–4379 (1972).
[18]M. Moskovits, "Surface-enhanced Raman spectroscopy: A brief retrospective," J. Raman Spectrosc. **36**, 485–496 (2005).
[19]D. Paria, K. Roy, H. J. Singh, S. Kumar, S. Raghavan, A. Ghosh, and A. Ghosh, "Ultrahigh field enhancement and photoresponse in atomically separated arrays of plasmonic dimers," Adv. Mater. **27**, 1751–1758 (2015).
[20]X. Li, W. C. H. Choy, X. Ren, D. Zhang, and H. Lu, "Highly intensified surface enhanced Raman scattering by using monolayer graphene as the nanospacer of metal film–metal nanoparticle coupling system," Adv. Funct. Mater. **24**, 3114–3122 (2014).
[21]M. E. Pumarol, M. C. Rosamond, P. Tovee, M. C. Petty, D. A. Zeze, V. Falko, and O. V. Kolosov, "Direct nanoscale imaging of ballistic and diffusive thermal transport in graphene nanostructures," Nano Lett. **12**, 2906–2911 (2012).
[22]K. I. Bolotin, K. J. Sikes, Z. Jiang, M. Klima, G. Fudenberg, J. Hone, P. Kim, and H. L. Stormer, "Ultrahigh electron mobility in suspended graphene," Solid State Commun. **146**, 351–355 (2008).
[23]R. R. Nair, P. Blake, A. N. Grigorenko, K. S. Novoselov, T. J. Booth, T. Stauber, N. M. R. Peres, and A. K. Geim, "Fine structure constant defines visual transparency of graphene," Science **320**, 1308 (2008).
[24]M. Montecchi and E. Masetti, "Measurement of vibrational deexcitation efficiencies of gold, chromium, zinc selenide, and amorphous carbon thin films," Phys. Rev. B **44**, 11649–11654 (1991).
[25]J. W. Suk, K. Kirk, Y. Hao, N. A. Hall, and R. S. Ruoff, "Thermoacoustic sound generation from monolayer graphene for transparent and flexible sound sources," Adv. Mater. **24**, 6342–6347 (2012).
[26]W. Zhao, W. Chen, Y. Yue, and S. Wu, "In-situ two-step Raman thermometry for thermal characterization of monolayer graphene interface material," Appl. Therm. Eng. **113**, 481–489 (2017).
[27]Y. Yue, J. Zhang, and X. Wang, "Micro/nanoscale spatial resolution temperature probing for the interfacial thermal characterization of epitaxial graphene on 4H-SiC," Small **7**, 3324–3333 (2011).
[28]B. M. Foley, S. C. Hernández, J. C. Duda, J. T. Robinson, S. G. Walton, and P. E. Hopkins, "Modifying surface energy of graphene via plasma-based chemical functionalization to tune thermal and electrical transport at metal interfaces," Nano Lett. **15**, 4876–4882 (2015).
[29]J. H. Seol, I. Jo, A. L. Moore, L. Lindsay, Z. H. Aitken, M. T. Pettes, X. Li, Z. Yao, R. Huang, D. Broido, N. Mingo, R. S. Ruoff, and L. Shi, "Two-dimensional phonon transport in supported graphene," Science **328**, 213–216 (2010).
[30]A. C. Ferrari, J. C. Meyer, V. Scardaci, C. Casiraghi, M. Lazzeri, F. Mauri, S. Piscanec, D. Jiang, K. S. Novoselov, S. Roth, and A. K. Geim, "Raman spectrum of graphene and graphene layers," Phys. Rev. Lett. **97**, 187401 (2006).
[31]G. Giovannetti, P. A. Khomyakov, G. Brocks, V. M. Karpan, J. van den Brink, and P. J. Kelly, "Doping graphene with metal contacts," Phys. Rev. Lett. **101**, 026803 (2008).
[32]V. Sutrová, I. Šloufová, Z. Melníková, M. Kalbáč, E. Pavlova, and B. Vlčková, "Effect of ethanethiolate spacer on morphology and optical responses of Ag nanoparticle array–single layer graphene hybrid systems," Langmuir **33**, 14414–14424 (2017).
[33]N. S. Mueller, S. Heeg, M. P. Alvarez, P. Kusch, S. Wasserroth, N. Clark, F. Schedin, J. Parthenios, K. Papagelis, C. Galiotis, M. Kalbáč, A. Vijayaraghavan, U. Huebner, R. Gorbachev, O. Frank, and S. Reich, "Evaluating arbitrary strain configurations and doping in graphene with Raman spectroscopy," 2D Mater. **5**, 015016 (2017).
[34]F. Schedin, E. Lidorikis, A. Lombardo, V. G. Kravets, A. K. Geim, A. N. Grigorenko, K. S. Novoselov, and A. C. Ferrari, "Surface-enhanced Raman spectroscopy of graphene," ACS Nano **4**, 5617–5626 (2010).
[35]S. T. Malak, T. König, R. Near, Z. A. Combs, M. A. El-Sayed, and V. V. Tsukruk, "Stacked gold nanorectangles with higher order plasmonic modes and top-down plasmonic coupling," J. Phys. Chem. C **118**, 5453–5462 (2014).
[36]M. Moskovits, "Persistent misconceptions regarding SERS," Phys. Chem. Chem. Phys. **15**, 5301–5311 (2013).
[37]Z.-Y. Guo and Z.-X. Li, "Size effect on single-phase channel flow and heat transfer at microscale," Int. J. Heat Fluid Flow **24**, 284–298 (2003).
[38]Z. Huang, J. Wang, S. Bai, J. Guan, F. Zhang, and Z. Tang, "Size effect of heat transport in microscale gas gap," IEEE Trans. Ind. Electron. **64**, 7387–7391 (2017).